The Explicit Wake Parametrisation V1.0: a wind farm parametrisation in the mesoscale model WRF

P. J. H. Volker, J. Badger, A. N. Hahmann, and S. Ott

Wind Energy Department, Technical University of Denmark, Risø Campus, Roskilde, Denmark

Correspondence to: P. J. H. Volker (pvol@dtu.dk)

Abstract

We describe the theoretical basis, implementation and validation of a new parametrisation that accounts for the effect of large offshore wind farms on the atmosphere and can be used in mesoscale and large-scale atmospheric models. This new parametrisation, referred to as

5 the Explicit Wake Parametrisation (EWP), uses classical wake theory to describe the unresolved wake expansion. The EWP scheme is validated for a neutral atmospheric boundary layer against filtered in situ measurements from two meteorological masts situated a few kilometres away from the Danish offshore wind farm Horns Rev I. The simulated velocity deficit in the wake of the wind farm compares well to that observed in the measurements

10 and the velocity profile is qualitatively similar to that simulated with large eddy simulation models and from wind tunnel studies. At the same time, the validation process highlights the challenges in verifying such models with real observations.

1 Introduction

Wind turbines capture the kinetic energy of the wind with their turning blades, which transfer

15 the energy to a transmission system that drives an electric generator. In this process the flow in front and behind a wind turbine is decelerated by the forces acting on the rotating blades. In large wind farms, the interaction of the flow and the wind turbines is further complicated by the interaction of the wake of one wind turbine with neighbouring turbines. Besides the changed velocity field around the turbines, there is also evidence that wind

20 turbines affect planetary boundary layer (PBL) processes due to the changed turbulence (Baidya Roy et al., 2004; Calaf et al., 2010; Baidya Roy and Traiteur, 2010; Barrie and Kirk-Davidoff, 2010; Wang and Prinn, 2010; Lu and Porté-Agel, 2011; Hasager et al., 2013; Fitch et al., 2013a).

Coastal regions are expected to become major areas for wind energy production, since

25 winds there are generally strong, steady, and less turbulent. To obtain an optimal yield, which is among others a function of power production, electrical cabling, and installation

2

costs, it is often convenient to group wind farms together. Examples are the Danish Rød-sand 2 and Nysted or the Belgian Belwind, Northwind, and Thornton wind farms, in which the wind farm separation is only a few kilometres. In planning new wind farms near existing ones it is important to estimate the velocity perturbation from the nearby farm as accurately

5 as possible, because the power production is highly sensitive to the wind speed. Veloc-ity deficits behind wind farms can be considerable. Christiansen and Hasager (2005), for example, found for near neutral atmospheric stability, velocity deficits of 2 % up-to 20 km downstream of the Horns Rev I ($25\,\mathrm{km}^2$) wind farm. The accurate measurement of wakes from nearby farms becomes even more important in light of the fact that as of 2015 large

10 offshore wind farms cover areas of up-to $100\,\mathrm{km}^2$. Mesoscale models are suitable tools to estimate wind energy resources in these sea areas (Hahmann et al., 2014). However, the collective effect of the wind turbines to the flow needs to be included in these models and because these occur at scales smaller than the model's grid-size and remain unresolved, the effects have to be parametrised.

15 The parametrisation of the effect of wind turbines largely depends on the model and its mesh size. For instance Large Eddy Simulation (LES) models, while resolving the local flow around wind turbines, need to parametrise the local drag forces on the turbine blade (Porté-Agel et al., 2011; Wu and Porté-Agel, 2013). The grid spacing of mesoscale models, on the other hand, is on the order of kilometres and tens of metres in the horizontal and vertical

20 direction, respectively. This means that the profile of the turbine-induced velocity deficit can be captured to some extent in the vertical direction. However, the downstream development of the velocity remains completely unresolved for scales smaller than the grid size. The major challenge in the parametrisation is to account for the unresolved relevant processes in agreement with the flow equations of the model. In recent years, steady progress has been

25 made in the parametrisation of the effect of wind farms in global and mesoscale models: from the representation of wind farms by an increased roughness length in Keith et al. (2004) and Frandsen et al. (2009), up-to the more advanced drag approaches in Adams and Keith (2007); Blahak et al. (2010); Baidya Roy (2011); Jacobson and Archer (2012); Fitch et al. (2012, 2013b), and Abkar and Porté-Agel (2015). Apart from a local drag force,

an additional turbulence Kinetic Energy (TKE) source term is assumed in the schemes proposed by Adams and Keith (2007); Blahak et al. (2010); Fitch et al. (2012), and Abkar and Porté-Agel (2015).

In this article we develop a new approach, which is hereafter referred to as Explicit Wake
[5] Parametrisation (EWP). We define the TKE from random fluctuations around the ensemble-averaged velocity, instead of around the grid-cell averaged velocity as done in the previous parametrisations. Therefore, to be consistent with the flow equations of the model, we apply a grid-cell averaged drag force and additional TKE is only provided by the PBL scheme where there is an increased vertical shear in horizontal velocity compared to the free-stream
[10] velocity profile.

We implemented the EWP scheme in the open source Weather Research and Forecast (WRF) model (Skamarock et al., 2008). The WRF model already includes a wind farm parametrisation option (Fitch et al., 2012), denoted as WRF-WF, which has been validated against wind farm measurements (Jiménez et al., 2014). We validated the WRF-WF and
[15] EWP parametrisations against long-term meteorological (met) mast measurements in the wake of an offshore wind farm. To our knowledge, measurements in the wake of a wind farm have not been used for the validation of a wind farm parametrisation model in previous literature.

In Sect. 2, we explain the theoretical basis of the EWP scheme and its implementation
[20] in the WRF model. Section 3 describes the measurements, whereas Sect. 4 introduces the WRF model set-up and the configuration of the EWP and WRF-WF scheme. In Sect. 5 both wind farm parametrisations are validated against the met mast measurements in the wake of the wind farm. A discussion of the results finalises the article in Sect. 6, followed by the conclusions in Sect. 7.

[25] 2 The Explicit Wake Parametrisation

We start by introducing the relevant mesoscale model equations. Thereafter, the additional terms that represent the effect of the the wind turbines are derived and added to the model

4

equations. At the end of the section their implementation in the mesoscale model is described.

2.1 The mesoscale model framework

Wind turbines are well described by drag devices that slow down the wind velocity from a free-stream value u. Downstream, due to mixing of fluid particles from within and outside the wake, the velocity deficit is gradually reduced to the point at which the background conditions are restored.

We use a mesoscale model for the simulation of the wind farm wake and its recovery. It uses the Reynolds Averaged Navier–Stokes (RANS) equations,

$$\frac{\partial \overline{u}_i}{\partial t} + \overline{u}_j \frac{\partial \overline{u}_i}{\partial x_j} + \frac{\partial \overline{u'_i u'_j}}{\partial x_j} = -\frac{1}{\rho} \frac{\partial \overline{p}}{\partial x_i} - 2\varepsilon_{ijk}\Omega_j \overline{u}_k - \delta_{i3} g + \overline{f}_{d_i}, \tag{1}$$

to describe the flow evolution. We use an over-line to denote ensemble-averaged quantities and a prime for a fluctuation around the ensemble average. The exception is the average air density $\rho(\boldsymbol{x},t)$, where t denotes the time and $\boldsymbol{x}$ the position. In Eq. (1), $\overline{u}_i(\boldsymbol{x},t)$ and $\overline{p}(\boldsymbol{x},t)$ represent the mean velocity components and the pressure, whereas Ω_j and g are the earth's rotation vector and the gravitational acceleration constant. Furthermore, the right most term $\overline{f}_{d_i}(\boldsymbol{x},t)$ is the ensemble-averaged horizontal forcing due to the action of wind turbines ($\overline{f}_{d_3} = 0$).

Mesoscale models generally simulate the effects of turbulence in the vertical direction only. The components of the Reynolds stress are parametrised in a 1.5-order PBL scheme as

$$\overline{u'_i u'_3} = -K_m \frac{\partial \overline{u}_i}{\partial x_3}, \tag{2}$$

where the turbulence diffusion coefficient for momentum, $K_m(\boldsymbol{x},t) = S_m \ell \left(\overline{u'_i u'_i} \right)^{\frac{1}{2}}$, depends on the stability function $S_m(\boldsymbol{x},t)$, the turbulence length scale $\ell(\boldsymbol{x},t)$, and the TKE

5

per unit mass, $\overline{u_i' u_i'}/2$. We write the most general form of the TKE equation:

$$\frac{\partial \overline{e}}{\partial t} + \overline{T} = \overline{p}_s + \overline{p}_b + \overline{p}_t - \epsilon, \tag{3}$$

where on the left hand side (l.h.s.) $\overline{e}$ denotes the TKE and $\overline{T}$ the transport, which includes the advection by the mean flow, turbulence transport of TKE and the divergence of the pressure correlation. On the right hand side (r.h.s.), $\overline{p}_s$ represents the turbulence production from the vertical shear in the horizontal velocity (shear production), $\overline{p}_b$ the turbulence production or destruction related to buoyancy forces, $\overline{p}_t$ the turbulence induced by the turbine rotor, and ϵ the dissipation.

2.2 The mesoscale model grid

For the mesoscale model, the previously defined variables in the Eqs. (1) and (3) have to be redefined on the three-dimensional model grid. For the parametrisation, we aim to obtain expressions for the volume-averaged drag force, $\langle \overline{f}_d \rangle$, and the volume-averaged turbulence induced by the turbine, $\langle \overline{p}_t \rangle$, that are consistent with the mesoscale model flow equations. Here, the angle brackets denote the volume average.

A new volume-averaged velocity equation is derived by integrating Eq. (1) over the grid-cell volume. This gives the expression for $\langle \overline{f}_d \rangle$, which is derived in the following Sect. 2.2.1.

The derivation of the additional term $\langle \overline{p}_t \rangle$ depends on the definition of the velocity perturbation. Formally, a velocity perturbation is the difference between the instantaneous and ensemble-averaged velocity. For homogeneous flows, the spatial-averaged velocity can be used for the definition of a velocity fluctuation, since the ensemble average can be approximated by the spatial average. However, the flow around wind turbines is non-homogeneous and consequently the spatial and ensemble average deviate. This has been illustrated in Fig. 1. Double averaging (ensemble and spatial) allows to separate the

6

total kinetic energy into three components. The definition of the term $\langle \overline{p}_t \rangle$ in the TKE equation will then depend on which of the three components contribute to the mean and which to the turbulence kinetic energy. In Appendix A, we discuss in more detail the double averaging and the ways mean and turbulence kinetic energy can be described.

In the EWP scheme, we follow Raupach and Shaw (1982) and Finnigan and Shaw (2008) and define a turbulence fluctuation around the ensemble mean (Approach I in Appendix A). Therefore, we include only the random motion in the TKE.

With this definition, the additional term becomes $\langle \overline{p}_t \rangle = \langle \overline{u'_{i,h} f'_{d_i}} \rangle$, where h is the hub-height of the turbine. When we use for the drag force, $f_{d_i} = -\rho A_r c_t u_{i,h}^2 / 2$, where $c_t(u)$ is the thrust coefficient and A_r the rotor area, we obtain:

$$
\begin{aligned}
\langle \overline{p}_t \rangle &= \langle \overline{u_{i,h} f_{d_i}} \rangle - \langle \overline{u}_{i,h} \overline{f}_{d_i} \rangle \\
&= -\rho A_r c_t \langle \overline{(\overline{u}_{i,h} + u'_{i,h}) u_{i,h}^2} \rangle / 2 + \rho A_r c_t \langle \overline{u}_{i,h} \overline{u_{i,h}^2} \rangle / 2 \\
&\approx -\rho A_r c_t \langle \overline{u}_{i,h} \overline{u_{i,h}'^2} \rangle,
\end{aligned}
\tag{4}
$$

This term represents a sink of TKE due to the extraction of momentum. The magnitude of this term is much smaller than the additional term in the WRF-WF scheme (see Sect. 4.1.2). Therefore, the additional term $\langle \overline{p}_t \rangle$ is neglected in the EWP approach. Additional turbulence is generated by shear production, which we assume to be the dominant mechanism on the grid-cell average.

In the following sections, we derive the expression for the grid-cell averaged $\langle \overline{f}_d \rangle$.

2.2.1 The sub-grid wake expansion

The velocity deficit expansion in the vertical direction within one grid-cell is not negligible, which leads to flow decelerations that extend beyond the rotor swept area. This part of the wake expansion is not accounted for in the mesoscale model, hence we estimate it explicitly with a sub-grid scale (turbulence) diffusion equation. Then, a grid-cell averaged force is determined and added to the model RANS equations.

7

In this model, we assume the horizontal advection of velocity and the turbulence diffusion to dominate in Eq. (1). Considering first only the flow behind the turbine rotor, we obtain from Eqs. (1) and (2) the diffusion equation:

$$5 \quad \overline{u}_0 \frac{\partial}{\partial x} \left(\overline{u}_0 - \widehat{u} \right) = K \frac{\partial^2}{\partial z^2} \left(\overline{u}_0 - \widehat{u} \right) + K \frac{\partial^2}{\partial y^2} \left(\overline{u}_0 - \widehat{u} \right) \tag{5}$$

that describes the expansion of the velocity deficit, $\overline{u}_0 - \widehat{u}$, behind the turbine. Here, $\overline{u}_0 = |\overline{u}(h,t)|$ denotes the advection velocity at hub-height and $\widehat{u}(x)$ the unresolved velocity in the stream-wise direction x in the wake of the turbine. The turbulence diffusion, which causes the wake expansion, is described by a single turbulence diffusion coefficient $K(x,y,t) =$
10 $K_m(x,y,h,t)$ in Eq. (2) and is given by the PBL scheme in WRF.

2.2.2 The velocity deficit profile

We define the vertical structure of the velocity deficit as $\overline{u}_d = \overline{u}_s \xi$, where $\overline{u}_s(x)$ is the maximum velocity deficit at the centre of the wake and $\xi(x,y,z)$ a function that determines the wake expansion (Tennekes and Lumley, 1972). Equation (5) can be solved for the velocity
15 deficit profile:

$$\overline{u}_d = \overline{u}_s \exp\left[-\frac{1}{2} \left(\frac{z-h}{\sigma} \right)^2 - \frac{1}{2} \left(\frac{y}{\sigma} \right)^2 \right], \tag{6}$$

where the length scale, σ, that determines the wake expansion is

$$\sigma^2 = \frac{2K}{\overline{u}_0} x + \sigma_0^2. \tag{7}$$

Equation (6) describes the ensemble-averaged profile of the velocity deficit around hub-
20 height at a given point in the far wake (Tennekes and Lumley, 1972). Equation (7) represents the vertical wake extension, resulting from turbulent diffusion of momentum and it is similar to the solution of Eq. (4.29) in Wyngaard (2010) for the dispersion of plumes.

8

Normally, the turbine wake is divided into a near and far wake, where the far wake begins between 1 and 3 rotor diameters (Vermeer et al., 2003; Crespo and Hernández, 1996). In the parametrisation, we account for the near wake expansion in the initial length scale σ_o and describe the unresolved far wake expansion with Eq. (6).

We can find the velocity deficit profile for wind turbines by equating the total thrust to the momentum removed by the action of the wind turbine, i.e.,

$$\frac{1}{2}\rho\,c_t\,\pi\,r_o^2\,\overline{u}_o^2 = \int\limits_{-\infty}^{\infty}\int\limits_{-\infty}^{\infty}\rho\,\overline{u}_o\overline{u}_d\,\mathrm{d}z\,\mathrm{d}y = \rho\,\overline{u}_o\,\overline{u}_s 2\pi\,\sigma^2, \tag{8}$$

where r_o is the radius of the rotor. In Eq. (8), the l.h.s. represents the local forces at the rotor swept area, whereas the r.h.s. describes the equivalent distributed force for the expanded wake at any x. From the Eqs. (8) and (6), we find the velocity deficit profile for a specific thrust force,

$$\overline{u}_d = \frac{c_t\,r_o^2\,\overline{u}_o}{4\,\sigma^2}\exp\left[-\frac{1}{2}\left(\frac{z-h}{\sigma}\right)^2 - \frac{1}{2}\left(\frac{y}{\sigma}\right)^2\right]. \tag{9}$$

When we insert the velocity deficit of Eq. (9) in the second term of Eq. (8) and integrate in the cross-stream direction y, we have the integrated thrust profile

$$\overline{f}_d = \int\limits_{-\infty}^{\infty}\int\limits_{-\infty}^{\infty}\rho\,\overline{u}_o\overline{u}_d\,\mathrm{d}z\,\mathrm{d}y = \int\limits_{-\infty}^{\infty}\rho\sqrt{\frac{\pi}{8}}\frac{c_t\,r_o^2\,\overline{u}_o^2}{\sigma}\exp\left[-\frac{1}{2}\left(\frac{z-h}{\sigma}\right)^2\right]\mathrm{d}z. \tag{10}$$

The term on the r.h.s. within the integral describes the equivalent distributed thrust force in the vertical direction at any distance x. Next, we derive from Eq. (10) a single effective thrust force, which represents the average wake expansion within a grid-cell.

2.2.3 Turbine forcing in the mesoscale model

For the mesoscale model we derive an effective thrust force, which describes the average wake expansion within a grid-cell. Therefore, we first determine the effective velocity deficit

profile $\overline{u}_e$ by averaging the velocity deficit of Eq. (9) over the cross-stream direction y and over a downstream distance L that the wake travelled within the grid-cell. It is convenient to approximate this area-averaged velocity deficit profile by a Gaussian-shaped profile:

$$\overline{u}_e = \sqrt{\frac{\pi}{8}} \frac{c_t r_0^2 \overline{u}_0}{\sigma_e} \exp\left[-\frac{1}{2}\left(\frac{z-h}{\sigma_e}\right)^2\right] \cong \frac{1}{L}\int\limits_0^L \int\limits_{-\infty}^{\infty} \overline{u}_d\,\mathrm{d}y\,\mathrm{d}x. \tag{11}$$

In Appendix B, we compare the area-averaged velocity deficit profile to the approximated Gaussian-shaped profile. In Eq. (11), σ_e is the effective length scale that is related to the model grid-size,

$$\sigma_e = \frac{1}{L}\int\limits_0^L \sigma\,\mathrm{d}x = \frac{\overline{u}_0}{3KL}\left[\left(\frac{2K}{\overline{u}_0}L + \sigma_0^2\right)^{\frac{3}{2}} - \sigma_0^3\right]. \tag{12}$$

From the definition of the effective length scale, we can obtain the total effective thrust force $\overline{f}_e$ by substituting the length scale σ in Eq. (10), with the effective length scale σ_e. This gives

$$\overline{f}_e = \int\limits_{-\infty}^{\infty} \rho\sqrt{\frac{\pi}{8}} \frac{c_r r_0^2 \overline{u}_0^2}{\sigma_e} \exp\left[-\frac{1}{2}\left(\frac{z-h}{\sigma_e}\right)^2\right]\,\mathrm{d}z. \tag{13}$$

The grid-cell averaged acceleration for the model RANS equations, Eq. (1), is now obtained, when we divide Eq. (13) by the mass and apply the grid-cell volume. For every vertical model layer k, we obtain then from Eq. (13) the grid-cell averaged acceleration components,

$$\langle\overline{f}_{d_1}(k)\rangle = -\sqrt{\frac{\pi}{8}}\frac{c_t r_0^2 \overline{u}_0^2}{\Delta x\,\Delta y\,\sigma_e}\exp\left[-\frac{1}{2}\left(\frac{z-h}{\sigma_e}\right)^2\right]\cos[\varphi(k)] \tag{14}$$

and

$$\langle\overline{f}_{d_2}(k)\rangle = -\sqrt{\frac{\pi}{8}}\frac{c_t r_0^2 \overline{u}_0^2}{\Delta x\,\Delta y\,\sigma_e}\exp\left[-\frac{1}{2}\left(\frac{z-h}{\sigma_e}\right)^2\right]\sin[\varphi(k)] \tag{15}$$

10

in the x and y direction, respectively. In Eqs. (14) and (15), we use Δx and Δy for the horizontal grid-spacing in the x and y direction and $\varphi(k)$ for the wind direction. For the height $z(k)$, we use the height at the centre of layer k.

2.3 Implementation in the WRF model

We assume every turbine within a grid-cell to be positioned at its centre and use $L = \Delta x/2$ in Eq. (12). In the numerical model, Eqs. (14) and (15) are added to the numerical approximation of Eq. (1). Furthermore, Eq. (12) is used to determine the effective length scale σ_e of the vertical wake extension. At every time-step the total thrust force within a grid-cell is obtained from a superposition of the single turbine thrust forces.

To a first approximation, we use the grid-cell averaged velocity at hub-height, $\langle \overline{u}_{o,h} \rangle$, as the upstream velocity $\overline{u}_o$ for all turbines within the same grid-cell (see Sect. 6). The turbulence diffusion coefficient for momentum, K in Eq. (12), comes from the selected PBL scheme. The parametrisation, therefore, can be used with any PBL scheme. However, to be consistent with the assumptions used in the derivation of the wind farm parametrisation, a 1.5 order closure scheme with a turbulence shear production term is recommended. A practical description of how to use the EWP scheme in the WRF model is given in the section "Code availability" at the end of the paper.

3 Wind farm and measurements

3.1 The Horns Rev I wind farm and met masts

The parallelogram-shaped Horns Rev I wind farm is situated in the North Sea about 15 km West of the Danish coast (Fig. 2). It is made up of 80 Vestas V80 (2 MW) pitch controlled, variable speed turbines, resulting in a total rated wind farm capacity of 160 MW. The turbines have a swept area diameter of 80 m with the hub mounted at 70 m a.m.s.l. The equally-spaced turbines are placed in 10 columns from West to East and 8 rows from North to South, labelled C1–C10 and R1–R8 in Fig. 2b. The spacing between columns and rows is

11

560 m, which is equivalent to 7 turbine diameters. Hansen et al. (2012) describes in detail the various production data available at the wind farm, their quality filtering, and processing.

Turbine (C1,R7) is used as a reference turbine, since it is not affected by the wind farm wake under westerly flows; in Fig. 2b it is marked with the solid bullet. The wind speed for each turbine is estimated from the power production data, using the turbine specific power curve and the wind direction is obtained from the adjusted yaw angle (Hansen et al., 2012).

For the validation, we use data from two met masts, M6 and M7, whose positions are shown in Fig. 2b. The masts are located 2 and 6 km to the east of the eastern edge of the wind farm and are thus directly in its wake for westerly winds. The 70 m tall masts are identically equipped and their instrumentation includes high quality Risø cup anemometers for measuring wind speeds. The 10-min averaged data from the two masts, which are independent of the wind farm data, is used to validate the modelled wind speed reductions downstream from the wind farm.

3.2 Data selection and averaging for the validation

For the validation of the results of the model simulations, and especially because of the relatively large area-averaged fields in the mesoscale model, it is very important to ensure that measurements and model fields are comparable. This can be achieved by properly selecting the wind direction and wind speed interval at the reference turbine.

Regarding the wind direction selection, Gaumond et al. (2013) found at Horns Rev I, for narrow wind direction sectors, a higher measured turbine production compared to that estimated by wake models. Most likely this is related to wind direction variations, which, for small wind direction bins, exceed the bin size within the 10 min averaging period. Since these variations are not accounted for in the model, we follow the recommendation to average over a relatively large wind direction interval. Furthermore, it is important that the flow reaching the mast anemometers has passed through the wind farm, otherwise it does not characterise the wind farm wake. Therefore, we select velocities whose directions are at the reference turbine between 255 and 285°. As demonstrated in Fig. 2b, the flow from this sector is influenced by the wind farm wake.

12

In the period 2005 to 2009, we select the 10-min averaged wind speeds from 6.5 to 11.5 m s^{-1} at the reference turbine and bin them in 1 m s^{-1} intervals. In this range, we guarantee to be above the cut-in wind speed of the turbines (4 m s^{-1}) and below the wind
5 speed at which the control system starts to pitch the blades (13 m s^{-1}). To obtain as much data as possible, we do not filter the measurements on stability. For strong westerly winds, we expect the atmospheric stability near to the ground on average to be neutral (Sathe et al., 2011).

For every instance that the wind direction and wind speed at the reference turbine was
10 within the above described range, the wind speeds at M6 and M7 were accepted. Afterwards, the selected wind speeds were averaged for each wind speed bin and normalised by the average wind speed at the reference turbine $\overline{u}_{\mathrm{ref}}$ (Table 1).

4 WRF model configuration and averaging

In the simulations we used the WRF model V3.4. However, the WRF-WF parametrisation
15 has been updated to the version available in WRFV3.6. The model domain is set-up with 80 × 40 grid-cells, with a horizontal grid-spacing $\Delta x = \Delta y = 1120$ m. This horizontal grid-spacing, which is twice the turbine separation, guarantees a constant number of turbines per grid-cell in the flow direction. Equally to the Horns Rev I wind farm, the model wind farm contains 80 V80 turbines and extends over 5 grid-cells in the West–East and North–
20 South direction (Fig. 3a). The Vestas V80 thrust and power curves were used for the turbine parameters.

The model was run in an idealised case mode with open lateral boundary conditions (Skamarock et al., 2008, p. 51), Coriolis forcing and zero heat fluxes from the lower boundary. At the surface, the no slip condition holds. The total domain is located over water and we
25 prescribe a constant roughness length of $z_0 = 2 \times 10^{-4}$ m, which follows the World Meteorological Organization (WMO) standards. The friction velocity is obtained with the Charnock formula. The model simulations were run with the MYNN 1.5 order Level 2.5 PBL scheme

13

(Nakanishi and Niino, 2009), on which the WRF-WF scheme is dependent. These and other details of the model configuration are summarised in Table 2.

We ran simulations for 5 wind speed intervals and for 9 wind directions, ranging from 255 to 285°. Additionally, to investigate the sensitivity to the vertical resolution, we set-up three experiments with 40 (L40), 60 (L60), and 80 (L80) layers in the vertical direction. With these vertical resolutions there are 5, 7, and 10 grid-cell volumes intersecting with the turbine rotor as shown in Fig. 3b.

All 135 simulations (5 wind speeds, 9 wind directions, and 3 vertical resolutions) were initialised with a constant geostrophic wind in height in a dry and slightly stable atmosphere. After a four day integration period, the wind converged in the whole domain to a logarithmic neutral profile within a 650 m deep boundary layer. The boundary layer was capped by an inversion layer with a potential temperature gradient of around $6\,K\,km^{-1}$. Above the inversion layer the velocity remained independent of height. The atmospheric state of each of these 135 simulations was used to drive: a control simulation without wind farm parametrisation, a simulation with the WRF-WF scheme, and a simulation with the EWP scheme. We used the restart option in the WRF model to initialise these simulations.

Each control or wind farm simulation lasted one day, resulting in a total simulation length of five days. The wind speeds in the control simulations were 7, 8, 9, 10, and $11\,m\,s^{-1}$ at 70 m (hub-height) after 5 days of simulation. We ended up with the desired magnitude of the geostrophic wind by conducting several experiments with different initialisations.

To summarise, we performed simulations for 9 wind directions, 5 wind speeds, and 3 vertical resolutions, with and without wind farm parametrisation, which gives a total of 405 (3 times 135) simulations as outlined in Table 3. For the validation against the mast measurements, we averaged the model wind speeds over the 9 wind directions with a uniform direction distribution. We used the instantaneous wind speeds at the end of the simulation period for the validation. Similarly to the observations, we normalise the wind direction averaged wind speeds and hereafter simply refer to them as "velocity". The model wind speeds from the simulations without the wind farm were used to normalise the wind farm flow.

14

4.1 Wind farm parameters

4.1.1 The EWP scheme

We use the wind speeds, derived from the power production data of the turbines, to determine the initial length scale σ_0 in Eq. (12). To a first approximation the initial length scale is defined to be independent of the upstream conditions and it is therefore the same for all turbines. The initial length scale is assumed to scale with the rotor radius and accounts for the near wake expansion.

For this calibration, we selected turbine production data at time stamps when the derived upstream wind speed and wind direction at the reference turbine ranged from 8.5 to $9.5\,\mathrm{m\,s^{-1}}$ and from 255 to $285°$. This wind speed bin was selected, since it contains the most turbine observations. It has a minimum of 850 observations for a turbine at the eastern edge of the wind farm and a maximum of 1612 observations for a turbine in the first wind farm column. The difference in the selected number of observations results from the additional requirement that for a given turbine the local upstream turbines have to be operational, in order to guarantee wake losses. For the power production data obtained in this way, we used the power curve to derive the wind speed. The column averaged velocity was afterwards obtained by averaging over the inner 6 rows (R2–R7). The outer rows were excluded because they experience different wake conditions under various wind directions.

Similarly to the model experiments in Sect. 4, we performed simulations for 9 wind directions between 255 to $285°$ for the 3 vertical resolutions with a wind speed at hub-height of $9\,\mathrm{m\,s^{-1}}$. To determine the best fitting value, we varied for the EWP simulations the initial length scale for all turbines from $\sigma_0 = r_0$ to $\sigma_0 = 2\,r_0$, stepping with $\Delta r_0 = 0.1$. For the comparison to the measurements, the column-averaged wind speed was obtained by averaging over the 3 central wind farm grid-cells in the cross-stream direction.

The lines in Fig. 4 show the hub-height velocity from the simulations with $\sigma_0 = 1.7\,r_0$, which had the smallest overall bias compared to the measurements. Additionally, the coloured dots indicate the sensitivity to the initial length scale for $\sigma_0 = 1.5$ and $1.9\,r_0$. It shows the same velocity reduction for all 3 vertical resolutions. Consequently, the amount

15

of energy extracted by the turbines is independent of the vertical resolution. The simulations with an initial length scale $\sigma_o = 1.7 r_o$ follow the measured velocity reduction fairly well. We use this length scale for all simulations in Sect. 5.

4.1.2 The WRF-WF scheme

In the validation, we also include results from the wind farm parametrisation WRF-WF from WRF-V3.6. This parametrisation was introduced in WRFV3.3 by Fitch et al. (2012). In this approach, the grid-cell averaged force, $\langle \overline{f}_d \rangle$, is approximated by the local forcing term at the turbine rotor. It applies to every model level that intersects with the wind turbine blade sweep area a fraction of the total force. Thus the scheme simulates the local drag forces over the turbine rotor. The additional TKE source term is parametrised as

$$\langle \overline{p}_{t,\text{WRF-WF}} \rangle = \rho\, A_r\, (c_t - c_p) \langle \overline{|u|} \rangle^3 / 2, \tag{16}$$

here c_p is the power coefficient of the turbine and $\langle \overline{|u|} \rangle$ the absolute value of the grid-cell velocity. The application of one-dimensional theory (Hansen, 2003) on Eq. (16), gives $\overline{p}_{t,\text{WRF-WF}} = \rho\, A_r\, c_t\, a \langle \overline{|u|} \rangle^3 / 2$ for the additional TKE term. Here, a denotes the induction factor.

The same result, $\langle \overline{p}_{t,\text{WRF-WF}} \rangle = \rho\, A_r\, c_t\, a \langle \overline{|u|} \rangle^3 / 2$, is obtained by defining a velocity fluctuation as the difference between the grid-cell averaged velocity and the instantaneous velocity (Approach II in Appendix A). In Fig. 1, this velocity fluctuation has been denoted by u''. An analytical derivation can be found in Abkar and Porté-Agel (2015) (their Eq. 21, with their $\xi = 1$). In this definition of TKE, the turbine induced velocity reduction is counted as TKE. For the considered wind speeds the absolute value of $\langle \overline{p}_{t,\text{WRF-WF}} \rangle$ is around 30 times larger than $\langle \overline{p}_t \rangle$ defined in Eq. (4), which comes from the different definition of TKE in the two schemes. For example, for $10\,\mathrm{m\,s^{-1}}$ with $c_t = 0.79$, $c_p = 0.43$, and $\langle \overline{u_{i,h}'^2} \rangle = 0.7\,\mathrm{m^2\,s^{-2}}$ at hub-height, the ratio between $\langle \overline{p}_{t,\text{WRF-WF}} \rangle$ and $\langle \overline{p}_t \rangle$ as it has been defined in Eq. (4) is 32.

In Sect. 5, we use the updated WRF-WF parametrisation from WRFV3.6, which has no free parameters. The power and thrust coefficients come from the Vestas V80 turbine.

16

5 Validation of the wind farm parametrisations

To obtain a complete picture of the modelled velocity field within and downstream of the Horns Rev I wind farm, we compare: (I) the velocity decay in the wake of the wind farm from the two wind farm parametrisations to the measurements for the $10\,\mathrm{m\,s^{-1}}$ wind speed bin. (II) the modelled velocities to the measurements at M6 (2 km downstream) and M7 (6 km downstream) for all five wind speeds (7, 8, 9, 10, and $11\,\mathrm{m\,s^{-1}}$). We recall that the initial length scale used in the EWP scheme has been determined for $9\,\mathrm{m\,s^{-1}}$.

In a qualitative validation, we examine the velocity reduction behind the wind farm and the profile of the velocity deficit. Furthermore, we discuss the vertical structure of the modelled TKE field from the discretized Eq. (3), where the additional term $\langle \overline{p_t} \rangle$ has been parametrised in the WRF-WF scheme and neglected in the EWP scheme. We use results from independent LES simulations and wind tunnel experiments as a reference.

In the validation, we use the instantaneous model outputs from the converged flow field after the 5 days integration period. Furthermore, the velocities are normalised as described in the Sects. 3 and 4.

5.1 Velocity recovery at turbine hub-height

Figure 5 shows the wind direction averaged hub-height velocity ($10\,\mathrm{m\,s^{-1}}$ bin) as a function of the downstream distance for the EWP and WRF-WF schemes and all vertical resolutions. For the EWP scheme (Fig. 5a) there is no identifiable vertical resolution dependency on the velocity, while for the WRF-WF (Fig. 5b) this is small. In the EWP scheme the velocity within the wind farm decreases almost linearly with distance. On the other hand, in the WRF-WF scheme it decreases more rapidly in the first turbine columns and becomes nearly constant with distance at the end of the wind farm. The behaviour in the EWP scheme suggests that no equilibrium has been reached within the wind farm between the extracted momentum by the wind turbines and the compensating flux of momentum from above. On the other hand, from the nearly constant velocity at the end of the wind farm for the WRF-WF scheme, it seems that the extraction of momentum by the turbines is almost balanced by the flux of

17

momentum from aloft. At the end of the wind farm the velocity difference between the two schemes is only 0.1 %. We have indicated the velocity from the EWP scheme at the most easterly grid-cell of the wind farm with a dotted horizontal line in Fig. 5. This agreement

5 is noteworthy, given the two different methods used. At M6, 2 km downstream of the wind farm, the modelled velocity for both schemes is within the uncertainty of the measurements. Nevertheless, the difference between the schemes is increased from 0.1 % at the end of the wind farm to 4.7 % at M6. This means that downstream of the wind farm grid-cells, where the wind farm parametrisations are not active, the velocity diverges for the two schemes

10 and its difference becomes significant. The near wake recovery is important, especially if the velocity was used to estimate the power production on a neighbouring wind farm that was located at this distance from the original wind farm. For example, the Rødsand 2 and Nysted offshore wind farm in Southern Denmark are separated by a comparable distance.

Figure 6 depicts wind direction averaged velocity recovery at the two met masts for all 5

15 wind speed bins and all vertical resolutions. It shows the differences in the WRF-modelled and measured wind speed at M6 (circles) and M7 (triangles), against the measured wind speed at the same masts. The WRF-modelled wind speed is obtained from linear interpolation of the wind speeds in the nearest grid-cells. The modelled recovery rate can be deduced from the slopes of the solid (between the values at M6 and M7) and dashed lines

20 (between M7 and the free-stream velocity). A negative slope is linked to a slower modelled recovery compared to that measured, whereas a positive slope shows a faster modelled recovery. There is no vertical resolution dependency for a wind farm parametrisation when the circles or triangles for a given wind speed bin lie on top of each other.

The results show that the bias in velocity between the measurements and the EWP sim-

25 ulations is small ($< 0.15\,\mathrm{m\,s^{-1}}$) for all wind speeds (except for the $7\,\mathrm{m\,s^{-1}}$ bin at M7). For the EWP scheme, we find a positive velocity difference at M6 and a negative one at M7. Hence, the modelled wake recovery oscillates between being slightly slower from M6 to M7 and being slightly faster from the end of the wind farm to M6, as well as from M7 to the end of the wake. The velocity of the EWP scheme at M6 is nearly independent of the vertical resolution and at M7 the dependency is very weak.

18

The WRF-WF scheme shows a positive difference in velocity of up-to $0.5\,\mathrm{m\,s^{-1}}$ at M6. This difference, between the WRF-WF scheme and the measurements, becomes larger with increasing wind speed. The higher modelled velocity at M6 is a consequence of the more rapid recovery of the modelled wake compared to that of the measurements from the end of the wind farm to M6. Between M6 and the point at which the free-stream velocity is reached again, the modelled wake recovery is slower than that measured. This overall positive difference suggests that the modelled velocity with the WRF-WF scheme is over-estimated throughout the whole wake.

Figure 7 shows the spatial structure of the modelled velocity ($10\,\mathrm{m\,s^{-1}}$ bin) within and in the wake of the wind farm for the L60 simulations in the $270°$ wind direction. A comparison of the results from the two schemes confirms the faster initial wind farm wake recovery in the WRF-WF scheme. The $10\,\%$ velocity deficit contour, for example, extends for the EWP scheme to around $x = 15\,\mathrm{km}$ (Fig. 7a), while for the WRF-WF scheme to $x = 8\,\mathrm{km}$ (Fig. 7b). The difference in the distance at which a $7.5\,\%$ velocity deficit is reached is even larger: after $x = 21$ and $x = 11\,\mathrm{km}$ for the EWP and WRF-WF scheme, respectively. Further downstream, after around $30\,\mathrm{km}$, the velocity fields from the two parametrisations become similar. Possible reasons for the difference in the initial wake recovery are discussed in the next section.

Finally, Fig. 7 shows a difference in the orientation of the axis of the velocity deficit downstream from the wind farm. In both simulations the steady-state wind direction of the free-stream flow was $270°$. As the velocity decreases within the wind farm, the velocity is expected to turn to the North, due to the changed Coriolis force. In the wind farm wake, where the flow accelerates again, the velocity should turn back again to the background direction. This effect is seen for the EWP scheme (Fig. 7a). Whereas, for the WRF-WF scheme (Fig. 7b) the wake turns southward behind the wind farm. A possible reason for this unexpected behaviour is the turbulence transport of momentum from aloft (Ekman spiral) within the wind farm. In the wind farm wake the flow keeps turning to the South because of the flow acceleration from the momentum transport.

5.2 Vertical profile of TKE and velocity

To obtain a broader understanding of the mechanisms acting in the two schemes, we compare the simulated TKE (per unit mass) and the velocity deficit profiles for the 10 m s^{-1} wind
5   speed bin in the 270° wind direction.

Figure 8 shows the difference in TKE (wind farm minus control simulation) for the L60 simulation. The cross-sections in the $x,\ z$ plane are in the West–East direction and pass through the centre of the wind farm. We used different colour scales in the two plots, due to the relatively large differences in TKE production between the two schemes. However,
10   we have kept the outermost contour (0.02 m^2 s^{-2}) the same. The maximum TKE difference was 0.30 and 1.9 m^2 s^{-2} for the EWP and WRF-WF scheme, respectively.

Compared to the environmental TKE of the pure shear flow (not shown), the TKE increases in the EWP scheme (Fig. 8a) at the end of the wind farm by a factor of 2, whereas in the WRF-WF scheme (Fig. 8b) it increases at hub-height by a factor of 5.5. The EWP
15   scheme shows an increased and decreased TKE above and below hub-height compared to the reference simulation. The maximum increase occurs behind the wind farm, where the velocity gradients are the largest. In the WRF-WF scheme, the maximum TKE increase happens at hub-height within the wind farm. Recalling that in the WRF-WF scheme, turbulence is generated by the source term $\langle \overline{p}_t \rangle$ and by the PBL scheme from turbulence shear
20   production ($\langle \overline{p}_s \rangle$), the intensity of $\langle \overline{p}_t \rangle$ dominates over that of the shear production. The sum of the additional source term and the turbulence shear production, causes within the wind farms an increased turbulence from the lowest model level upwards.

We use the results from the actuator disk approach without rotation from Wu and Porté-Agel (2013), to obtain a qualitative impression of the structure of the turbulence field from
25   a LES model within a wind farm. The actuator disk approach from their LES model is most similar to the drag approach in the mesoscale model. Their Fig. 5c shows that higher and lower turbulence intensities dominate around the upper and lower turbine blade tip. Also, a positive and negative shear stress occur above and below hub-height (their Fig. 7c). This indicates that the shear in velocity dominates the turbulence production. Similar features are

present in the TKE field from the EWP scheme, where the increased and decreased TKE above and below hub-height are in like manner caused by an enhanced and reduced turbulence shear production with respect to the neutral logarithmic velocity profile. Furthermore,
5 Wu and Porté-Agel (2013) shows an upper wake edge at around 4.5 turbine hub-heights for 10 aligned wind turbines after 60 turbine diameters (their Fig. 12). They defined the wake edge at the point where the velocity reduction for a given height was 1 %. Similarly, the edge of the wake can be found from an increased TKE due to shear production. For the outermost contour in Fig. 8, we obtain a vertical wake extension of around 5 turbine
10 diameters for the EWP scheme at 4.8 km downstream (equivalent to 60 turbine diameters). At the same distance, it is around 7 turbine hub-heights for the WRF-WF scheme.

The influence of the TKE field to the velocity profile is analysed in Fig. 9. It shows the velocity deficit profile $\Delta\langle\overline{u}_x\rangle/\langle\overline{u}_{\mathrm{o},h}\rangle$ for both schemes and all vertical resolutions. Here $\langle\overline{u}_{\mathrm{o},h}\rangle$ denotes the free-stream velocity at hub-height. The velocity deficit is defined as
15 $\Delta\langle\overline{u}_x(z)\rangle = \langle\overline{u}(z)\rangle - \langle\overline{u}_{\mathrm{free}}(z)\rangle$, where $\langle\overline{u}_{\mathrm{free}}(z)\rangle$ is the free-stream velocity profile from the reference simulation and $\langle\overline{u}(z)\rangle$ the velocity profile from the wind farm simulation. The free-stream velocities from the EWP and WRF-WF simulations were visually indistinguishable. We choose the second and third grid-cell within the wind farm (C2 and C3) and the second point behind the wind farm (C7) that corresponds approximately to the location of M6.

20 Figure 9a shows the velocity deficit profiles from the EWP and WRF-WF scheme from the L60 simulation. The profiles indicate a stronger diffusion in the WRF-WF scheme compared to that in the EWP scheme. This can be recognised by the vertical extension of the vertical deficit profile at C7, behind the wind farm.

For the EWP scheme (Fig 9b), we find a maximum velocity deficit at hub-height and sym-
25 metric features around the maximum for the L40 and L80 simulations. Also, results from LES simulations, wind tunnel experiments, and measurements (Vermeer et al., 2003; Wu and Porté-Agel, 2013; Iungo et al., 2013) have a maximum velocity deficit at hub-height in the far turbine wake for a neutral boundary layer. The profiles in Vermeer et al. (2003) (their Fig. 36) and in Wu and Porté-Agel (2013) (their Fig. 4) additionally show symmetric features around the maximum with a shape similar to the velocity profile of the EWP scheme. Fig-

21

ure 9b demonstrates the vertical resolution independence of the EWP scheme within the wind farm: the velocity deficits of the L40 and L80 simulations are almost identical. A small difference is found below hub-height in the wind farm wake.

⁵ With the WRF-WF scheme (Fig. 9c) the maximum velocity deficit is displaced vertically above hub-height, which reaches the upper wind turbine blade tip at mast M6 (C7). The dependency of WRF-WF scheme to the chosen vertical resolutions is weak; differences are found within the wind farm (C2, C3) above hub-height. Also, the profiles from the WRF-WF scheme show increased (area-averaged) velocities inside the wind farm at the lowest
¹⁰ model level. The wind farm simulations from Wu and Porté-Agel (2013) (their Fig. 13) do not support this behaviour.

6 Discussion

We use wind farm parametrisations implemented in a mesoscale models to simulate the effect of wind farm wakes in areas on the order of hundreds of kilometres. However, the
¹⁵ models have a limited horizontal resolution and hence the local processes within a wind farm remain unresolved. In the proposed parametrisation, we use the classical wake theory (Tennekes and Lumley, 1972) to describe the sub-grid-scale wake expansion. Compared to empirical fits from for example Xie and Archer (2014) and Zang et al. (2013), it offers the advantage that the wake expansion is described as a function of atmospheric stability. In this
²⁰ study, we have validated the approach for different wind speeds in a neutral atmospheric boundary layer. Its performance as a function of atmospheric stability, which requires information of the profiles, will be investigated in future. Wu and Porté-Agel (2013) found in their LES model results a sensitivity of the velocity reduction to the wind farm layout. In current implementations of wind farm parametrisations, all turbines within a grid-cell experience the
²⁵ same upstream velocity. Although these parametrisations are not meant to estimate the local velocity field within the wind farm, differences in velocity reduction within the wind farm could affect the velocity in the wake of it. Future implementations may account for the local flow within the wind farm by using data from high resolution models, which can be input to

22

the mesoscale model via a look-up table as suggested by Badger et al. (2013) and Abkar and Porté-Agel (2015). However, we have at the moment no measurement data in the wind farm wake to validate these approaches for different wind farm layouts. At the Horns Rev I
5 wind farm, we were restricted to the geometry of met masts positions, which did not allow to study the sensitivity of the velocity field in the wind farm wake for additional wind direction sectors.

A fair comparison between the mesoscale model and long-term measurements can be realised in several ways. One method is to match the simulation period to that observed.
10 By selecting corresponding time frames, one can then compare the fields of interest. The main disadvantage of this method is that errors in the background flow simulated by the mesoscale model also exist, which complicates the analysis. The second method is to sample the data and the model simulations in rather strict idealised conditions of wind speed and direction. We have chosen this second method using the WRF model in idealised case
15 mode and compare its results to properly averaged measurements. Here the equilibrium solution without the wind farm effects is purposely made to match the free stream velocity and thus background errors in the simulations are absent. Besides a more detailed analysis, this method also allows the study of the vertical dependency of the velocity reductions, since the atmospheric background conditions are almost identical for the simulations with
20 different vertical resolutions.

Before we validated the results of the schemes in the wake of the wind farm, the a priori unknown initial length scale of the EWP scheme had to be determined. We did this using the turbine power measurements from the most frequently observed wind speed bin. This limitation could not be avoided, since to our knowledge no other long-term measurements
25 from large offshore wind farms are available. We found for the most frequently observed wind speed bin an initial length scale of $\sigma_0 = 1.7 r_0$ that fitted the turbine measurements the best. We recommend this constant for similar wind turbines. Future wind turbine measurements are needed to determine this value for other turbine types, such as low induction turbines. This constant was then used for the validation of all wind speed bins. On the other hand, for the WRF-WF scheme we have used the turbine specific thrust and power curves,

which are its only input parameters. The difference of 0.1 % between the velocity deficit simulated by the WRF-WF and EWP scheme at the end of the wind farm for the $10\,\mathrm{m\,s^{-1}}$ wind speed bin, facilitated the comparison between the schemes in the wind farm wake, where the parametrisations are not active anymore.

One major difference between the EWP and WRF-WF approach is in the treatment of the grid-cell averaged TKE budget equation. The TKE production regulates the vertical profiles of momentum, temperature, and moisture within the PBL. Differences in TKE production would thus affect the local weather (e.g., temperature, humidity, and possibly clouds) response to the presence of large wind farms. Both wind farm schemes use a PBL scheme that parametrises the TKE equation in terms of grid-cell averaged variables. Therefore, in the wake of the wind turbines TKE is generated by the increased vertical shear in horizontal velocity. Then, the different definition of the unresolved velocity fluctuation in the WRF-WF and EWP scheme leads to a different term $\langle \overline{p}_t \rangle$ that is the direct consequence of the presence of a drag force. In the EWP scheme, a velocity fluctuation is defined around the ensemble-averaged velocity. With this definition $\langle \overline{p}_t \rangle$ is small and can be neglected. Instead, in the WRF-WF scheme velocity fluctuations are defined around the grid-cell averaged velocity and a parametrisation of $\langle \overline{p}_t \rangle$ is added to the model TKE equation. The simulations have shown that in the WRF-WF scheme $\langle \overline{p}_t \rangle$ dominates over the shear production and that its total TKE is more than 3 times larger than that in the EWP scheme. However, it is unclear how well the actual grid-cell averaged shear production is approximated by the shear production calculated with the PBL scheme in WRF, on which the EWP scheme relies. Therefore, future measurement campaigns of the actual structure and intensity of the TKE field within and around wind farms under suitable atmospheric conditions can help to settle this issue.

7 Conclusions

We introduce a wind farm parametrisation for use in mesoscale models. The EWP approach is based on classical wake theory and parametrises the unresolved expansion of

the turbine-induced wake explicitly in the grid-cell that contains turbines, where the largest velocity gradients occur. The associated turbulence shear production is then determined by the PBL scheme in the mesoscale model. The approach has been implemented in the WRF mesoscale model and can be used with any PBL scheme. However, we recommend PBL schemes that model the TKE equation.

We analysed the results of simulations from the scheme in the wake of a wind farm. For the validation, we used the averaged wind speeds within a 30° wind direction sector at two met masts in the wake of the Horns Rev I wind farm. The model was run for several wind direction bins that cover those sampled in the observations. For each wind speed bin, we compared a wind direction averaged wind speed to the similarly averaged measurements. We found that for all 5 velocity bins, the velocity modelled with the EWP scheme agreed well with the met mast measurements 2 and 6 km downstream from the edge of the wind farm. The EWP scheme reproduces the wind farm wake within the standard deviation of the measurements.

To our knowledge, no long-term data-sets are available to validate the details of the vertical structure of the velocity deficit and turbulence in the wake of the wind farm. In a qualitative comparison, we found the vertical structure of the modelled TKE field to agree with that of actuator-disk simulations by LES models (Wu and Porté-Agel, 2013), with an increased and decreased TKE around the upper and bottom rotor tip, respectively. The TKE field in the EWP scheme led to a symmetric velocity deficit profile around hub-height, similar to velocity deficit profiles in Wu and Porté-Agel (2013); Vermeer et al. (2003). Also, the vertical wind farm wake expansion in the EWP approach was similar to that described in the before mentioned studies. While validation of the WRF-WF parametrisation has before been carried out with measurements within a wind farm (Jiménez et al., 2014), this is the first time that the validation has been done in the wake of a wind farm, at the scales the mesoscale model was designed to simulate.

25

Appendix: A

We use the notation and symbols of Raupach and Shaw (1982), with the exception that the ensemble average is used instead of the time average. The instantaneous velocity, u_i, can be decomposed in a spatial average with a fluctuation around it, $u_i = \langle u_i \rangle + u_i''$ and an ensemble average with a fluctuation, $u_i = \overline{u}_i + u_i'$. Figure 1 illustrates the instantaneous velocity (grey line), as well as the spatial (red line) and ensemble-averaged (blue line) velocity in the vicinity of a wake.

We can decompose the total kinetic energy:

$$\frac{1}{2}\langle \overline{u_i^2} \rangle = \frac{1}{2}\langle \overline{u}_i^2 \rangle + \frac{1}{2}\langle \overline{u_i'^2} \rangle \tag{1}$$
$$= \frac{1}{2}\langle \overline{u}_i \rangle^2 + \frac{1}{2}\langle \overline{u_i''^2} \rangle + \frac{1}{2}\langle \overline{u_i'^2} \rangle. \tag{2}$$

In Eq. (1), we applied an ensemble and spatial averaging to the kinetic energy and we have decomposed the ensemble-averaged kinetic energy in an average and fluctuating part. Here, $\frac{1}{2}\langle \overline{u}_i^2 \rangle$ is the spatial average of the ensemble-averaged kinetic energy and $\frac{1}{2}\langle \overline{u_i'^2} \rangle$ the spatial average of the kinetic energy from random velocity fluctuations.

By decomposing the first term on the r.h.s. of Eq. (1), we obtain Eq. (2). In Eq. (2), we now have three contributions to the total spatial and ensemble-averaged kinetic energy. The first term $\frac{1}{2}\langle \overline{u}_i \rangle^2$ is the kinetic energy of the spatial and ensemble-averaged velocity. The second term $\frac{1}{2}\langle \overline{u_i''^2} \rangle$ is the spatial-averaged kinetic energy of the heterogeneous part of the mean flow, which is the difference between the ensemble and spatial-averaged kinetic energy. This term arises only in non-homogeneous flow conditions and is also called "dispersive kinetic energy" by Raupach and Shaw (1982).

For each contribution on the r.h.s. of Eq. (2) to the total kinetic energy, a budget equation can be derived. The complete set of equations can for example be found in Raupach and

Shaw (1982). We can combine the three components in Eq. (2) to kinetic energy of the mean flow (MKE) and turbulence kinetic energy (TKE). The MKE is not directly resolved by the model. However, the definition of TKE determines how the effect of wind turbines to the TKE is parametrised.

In approach I, one can define MKE = $\frac{1}{2}\langle \overline{u}_i^2 \rangle = \frac{1}{2}\langle \overline{u}_i \rangle^2 + \frac{1}{2}\langle \overline{u}_i''^2 \rangle$ and TKE = $\frac{1}{2}\langle \overline{u_i'^2} \rangle$ (Raupach and Shaw, 1982; Finnigan and Shaw, 2008). Here, the MKE is equal to the spatial average of the ensemble-averaged kinetic energy and it contains all kinetic energy of the organised motion. With this definition only random motion contributes to the TKE. The presence of the drag force gives rise to the term $\langle \overline{p}_t \rangle = \langle \overline{u_i' f_{d_i}'} \rangle$, where f' is the fluctuation of the drag force around the ensemble-averaged force. This approach is used in the EWP scheme and in Sect. 2.2 the additional term is derived.

In approach II, one could define MKE = $\frac{1}{2}\langle \overline{u}_i \rangle^2$ and then the TKE = $\frac{1}{2}\langle \overline{u}_i''^2 \rangle + \frac{1}{2}\langle \overline{u_i'^2} \rangle$. In this case, the MKE contains only kinetic energy from the spatial-averaged velocity. Whereas, the TKE contains now also energy from the heterogeneous part of the mean flow additional to the energy from random motion. In this approach, a fluctuation can be decomposed in $u'' = \overline{u}_i'' + u_i'$. Therefore, the source term becomes $\langle \overline{p}_t \rangle = \langle \overline{u_i'' f_{d_i}''} \rangle$, where f'' is the fluctuation of the drag force around the spatial averaged-force. In the WRF-WF, this approach is used (see Sect. 4.1.2).

Appendix: B

In the EWP scheme, we approximate the velocity deficit profiles on the r.h.s. of Eq. (11), by a Gaussian shaped velocity profile on the l.h.s. of Eq. (11).

To show that these profiles are to a good approximation similar, we compare the difference between the average of 5000 single profile at distances $0 < x < 500$ m to the approximated Gaussian velocity deficit. We normalise both profiles by the depth, Δy, of the wake in the

27

cross-stream direction. For the comparison we used $\overline{u}_o = 8\,\mathrm{m\,s^{-1}}$, $r_o = 40\,\mathrm{m}$, $\sigma_o = 60\,\mathrm{m}$, $c_T = 0.8$, $K = 6\,\mathrm{m^2\,s^{-1}}$, and $\Delta y = 1120\,\mathrm{m}$. The wake centre is defined at $z = 0\,\mathrm{m}$.

The result in Fig. 10 shows that the differences between the spatial averaged Gaussian profiles and the Gaussian profile with the space averaged spread is in the entire velocity deficit region far less than $0.001\,\mathrm{m\,s^{-1}}$.

Code availability

In this section a short guideline of the usage of the EWP scheme in the WRF model is given. The EWP approach can be run either in serial, shared-memory, or distributed memory options. Currently, it is not possible to run the approach with the mixed shared and distributed memory option. The scheme can be used for `idealised` and `real` case simulations. For the `real` case simulations, the wind farm parametrisation can be activated in any nest of the simulations. The additional namelist.input option `bl_turbine` should be used to select the wind farm parametrisation.

The EWP scheme needs additional input files in ASCII format. In the first file the positions and types of all wind turbines should be listed. The file name has to be specified as a string in the additional namelist.input option `windturbines_spec`. For every turbine used, the turbine characteristics, i.e., the hub-height and diameter, and the thrust and power coefficients as a function of wind speed, need to be listed in a file. The power coefficient is used optionally to estimate the turbine power production. This file name has to start with the turbine type used in the first file, followed by the extension `.turbine`.

Please contact pvol@dtu.dk to obtain the code of the EWP wind farm parametrisation.

The Supplement related to this article is available online at
doi:10.5281/zenodo.17109.

References

Abkar, M. and Porté-Agel, F.: A new wind-farm parameterization for large-scale atmospheric models, J. Renewable and Sustainable Energy, 7, 013121, doi:10.1063/1.4907600, 2015.

Adams, A. S. and Keith. D. W.: A wind farm parametrization for WRF, 8th WRF Users Workshop, 11–15 June 2007, Boulder, abstract 5.5, available at: http://www2.mmm.ucar.edu/wrf/users/workshops/WS2007/abstracts/5-5_Adams.pdf, 2007.

Badger, J., Volker, P. J. H., Prospathospoulos, J., Sieros, G., Ott, S., Rethore, P.-E., Hahmann, A. N., and Hasager, C. B.: Wake modelling combining mesoscale and microscale modelsm, in: Proceedings of ICOWES, Technical University of Denmark, 17–19 June 2013, Lyngby, p. 182–193, available at: http://indico.conferences.dtu.dk/getFile.py/access?resId=0&materialId=paper&confId=126, 2013.

Baidya Roy, S.: Simulating impacts of wind farms on local hydrometeorology, J. Wind Eng. Ind. Aerod., 99, 491–498, 2011.

Baidya Roy, S. and Traiteur, J. J.: Impact of wind farms on surface air temperature, P. Natl. Acad. Sci. USA, 107, 17899–17904, 2010.

Baidya Roy, S., Pacala, S. W., and Walko, R. L.: Can large wind farms affect local meteorology?, J. Geophys. Res., 109, 2156–2202, 2004.

Barrie, D. B. and Kirk-Davidoff, D. B.: Weather response to a large wind turbine array, Atmos. Chem. Phys., 10, 769–775, doi:10.5194/acp-10-769-2010, 2010.

Blahak, U., Goretzki, B., and Meis, J.: A simple parametrisation of drag forces induced by large wind farms for numerical weather prediction models, EWEC Conference, 20–23 April 2010, Warsaw, p. 186–189, available at: http://proceedings.ewea.org/ewec2010/allfiles2/757_EWEC2010presentation.pdf, 2010.

Calaf, M., Meneveau, C., Meyers, J.: Large eddy simulation study of fully developed wind-turbine array boundary layers, Phys. Fluids, 22, 015110, doi:doi:10.1063/1.3291077, 2010.

29

Christiansen, M. B. and Hasager, C. B.: Wake effects of large offshore wind farms identified from satellite SAR, Remote Sens. Environ., 98, 251–268, 2005.

Crespo, A. and Hernández, J.: Turbulence characteristics in wind-turbine wakes, J. Wind. Eng. Ind. Aerod., 61, 71–85, 1996.

Finnigan, J. J. and Shaw, R. H.: Double-averaging methodology and its application to turbulent flow in and above vegetation canopies, Acta Geophysica, 56, 534-561, doi:10.2478/s11600-008-0034-x, 2008.

Fitch, A. C., Lundquist, J. K., and Olson, J. B.: Mesoscale influences of wind farms throughout a diurnal cycle, Mon. Weather Rev., 141, 2173–2198, 2013a.

Fitch, A. C., Olson, J. B., and Lundquist, J. K.: Parameterization of Wind Farms in Climate Models, J. Climate, 26, 6439–6458. doi:doi: http://dx.doi.org/10.1175/JCLI-D-12-00376.1, 2013b.

Fitch, A. C., Olson, J. B., Lundquist, J. K., Dudhia, J., Gupta, A., Michalakes, J., and Barstad, I.: Local and mesoscale impacts of wind farms as parameterized in a mesoscale NWP model, Mon. Weather Rev., 140, 3017–3038, 2012.

Frandsen, S. T., Jørgensen, H. E., Barthelmie, R., Badger, J., Hansen, K. S., Ott, S., Rethore, P.-E., Larsen, S. E., and Jensen, L. E.: The making of a second-generation wind farm efficiency model complex, Wind Energy, 12, 445–458, 2009.

Gaumond, M., Réthoré, P.-E., Ott, S., Peña A., Bechmann, A., and Hansen, K. S.: Evaluation of the wind direction uncertainty and its impact on wake modeling at the Horns Rev offshore wind farm, Wind Energy, 7, 1169–1178, 2014.

Hahmann, A. N., Vincent, C. L., Peña, A., Lange, J., and Hasager, C. B.: Wind climate estimation using WRF model output: method and model sensitivities over the sea, Int. J. Climatol., published online, doi:10.1002/joc.4217, 2014.

Hansen, K. S., Barthelmie, R. J., Jensen, L. E., and Sommer, A.: The impact of turbine intensity and atmospheric stability on power deficits due to wind turbine wakes at Horns Rev wind farm, Wind Energy, 15, 183–196, 2012.

Hansen, M. O. L.: Aerodynamics of Wind Turbines, James & James, London, UK, 2003.

Hasager, C. B., Rasmussen, L., Peña, A., Jensen, L. E., and Réthoré, P.-E.: Wind farm wake: the Horns Rev Photo Case, Energies, 6, 696–716, 2013.

Iungo, G. V., Wu, Y.-T., and Porté-Agel, F.: Field measurements of wind turbine wakes with lidars, J. Atmos. Ocean. Tech., 30, 274–287, 2013.

Jacobson, M. Z. and Archer, C. L.: Saturation wind power potential and its implications for wind energy, P. Natl. Acad. Sci. USA, 109, 15679–15684, 2012.

Jiménez, P. A., Navarro, J., Palomares, A. M., and Dudhia, J.: Mesoscale modeling of offshore wind turbine wakes at the wind farm resolving scale: a composite-based analysis with the Weather Research and Forecasting model over Horns Rev, Wind Energy, 18, 559–566, 2014.

Keith, D. W., DeCarolis, J. F., Denkenberger, D. C., Lenschow, D. H., Malyshev, S. L., Pacala, S., and Rasch, P. J.: The influence of large-scale wind power on global climate, P. Natl. Acad. Sci. USA, 101, 16115–16120, 2004.

Lu, H., and Porté-Agel, F.: Large-eddy simulation of a very large wind farm in a stable atmospheric boundary layer, Phys. Fluids, 23, 065101, doi:doi:10.1063/1.3589857, 2011.

Nakanishi, M. and Niino, H.: Development of an improved turbulence closure model for the atmospheric boundary layer, J. Meteorol. Soc. Jpn., 87, 895–912, 2009.

Porté-Agel, F., Wu, Y.-T., Lu, H., and Conzemius, R. J.: Large-eddy simulation of atmospheric boundary layer flow through wind turbines and wind farms, J. Wind Eng. Ind. Aerod., 99, 154–168, 2011.

Raupach, M. R. and Shaw, R. H.: Averaging procedures for flow within vegetation canopies, Bound.-Lay. Meteorol., 22, 79–90, doi:10.1007/BF00128057, 1982.

Sathe, A., Gryning, S.-E., and Peña, A.: Comparison of the atmospheric stability and wind profiles at two wind farm sites over a long marine fetch in the North Sea, Wind Energy, 14, 767–780, 2011.

Skamarock, W., Klemp, J., Dudhia, J., Gill, D., Barker, D., Duda, M., Huang, X., Wang, W., and Powers, J.: A Description of the Advanced Research WRF Version 3, NCAR Technical note, Massachusetts, USA, 2008.

Tennekes, H. and Lumley, J. L.: A First Course in Turbulence, The MIT Pess, Boulder, USA, available at: http://www2.mmm.ucar.edu/wrf/users/docs/arw_v3.pdf, 1972.

Vermeer, L. J., Søensen, J. N., and Crespo, A.: Wind turbine wake aerodynamics, Prog. Aerosp. Sci., 39, 467–510, 2003.

Wang, C. and Prinn, R. G.: Potential climatic impacts and reliability of very large-scale wind farms, Atmos. Chem. Phys., 10, 2053–2061, doi:10.5194/acp-10-2053-2010, 2010.

Wu, Y.-T. and Porté-Agel, F.: Simulation of turbulent flow inside and above wind farms: model validation and layout effects, Bound.-Lay. Meteorol., 146, 181–205, 2013.

Wyngaard, J. C.: Turbulence in the Atmosphere, Cambridge Press, Cambridge, UK, 2010.

Xie, S., Archer, C.: Self-similarity and turbulence characteristics of wind turbine wakes via large-eddy simulation, Wind Energy (2014) doi:DOI: 10.1002/we.1792

Zhang, W., Markfort, C. D., and Porté-Agel, F.: Wind-Turbine Wakes in a Convective Boundary Layer: A Wind-Tunnel Study, Bound.-Lay. Meteorol. 146, 161–179, 2013 doi:DOI 10.1007/s10546-012-9751-4.

31

Table 1. Average wind speed at the reference turbine ($\overline{u}_{ref}$) and frequency of the measurements at the met mast for all wind speed bins within the wind direction range 255–285°.

Wind speed bin $(m\,s^{-1})$	$\overline{u}_{ref}$ $(m\,s^{-1})$	N_{obs} at M6–M7
7 ± 0.5	7.00	887
8 ± 0.5	7.95	933
9 ± 0.5	8.95	1097
10 ± 0.5	10.05	990
11 ± 0.5	11.05	729

Table 2. The WRF model configuration used in the simulations.

Number of grid-cells in the horizontal plane (nx, ny):	80, 40
Horizontal grid spacing (km):	1.12
Domain size in x, y, z (km):	89.6, 33.6, 15
Wind farm extension ($nx \times ny$):	5×5
Boundary condition:	OPEN
PBL scheme:	Nakanishi and Niino (2009)
Surface layer scheme:	MYNN Monin-Obukhov similarity theory
TKE advection:	Yes
Pert Coriolis:	Yes
Roughness length (m):	2×10^{-4}
Coriolis frequency (s^{-1})	1.2×10^{-4}

Table 3. Details of the WRF simulations.

Wind direction range (°):	258.75–281.25
Wind direction interval (°):	3.75
Wind speeds (m s^{-1}):	7.0, 8.0, 9.0, 10.0 and 11.0
Number of vertical levels (nz):	40 (L40), 60 (L60), 80 (L80)
Wind farm parametrisation:	None, WRF-WF, EWP
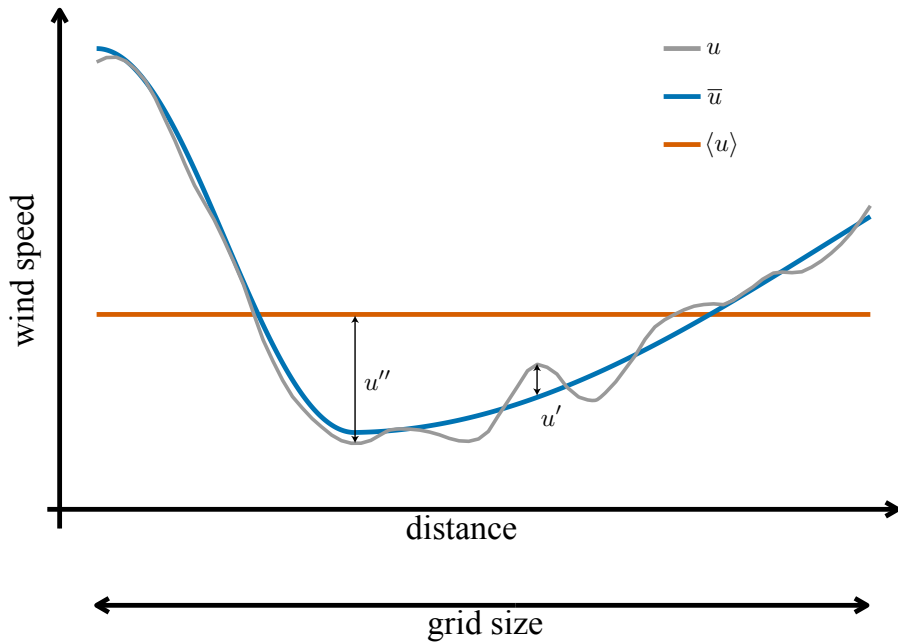
Figure 1. A sketch of the downstream development of a turbine induced velocity reduction. The x-axis indicates the grid-cell size. The grey line represents the instantaneous velocity and the coloured lines the averaged values. The difference between the average and instantaneous velocity defines the turbulence fluctuation at each distance.
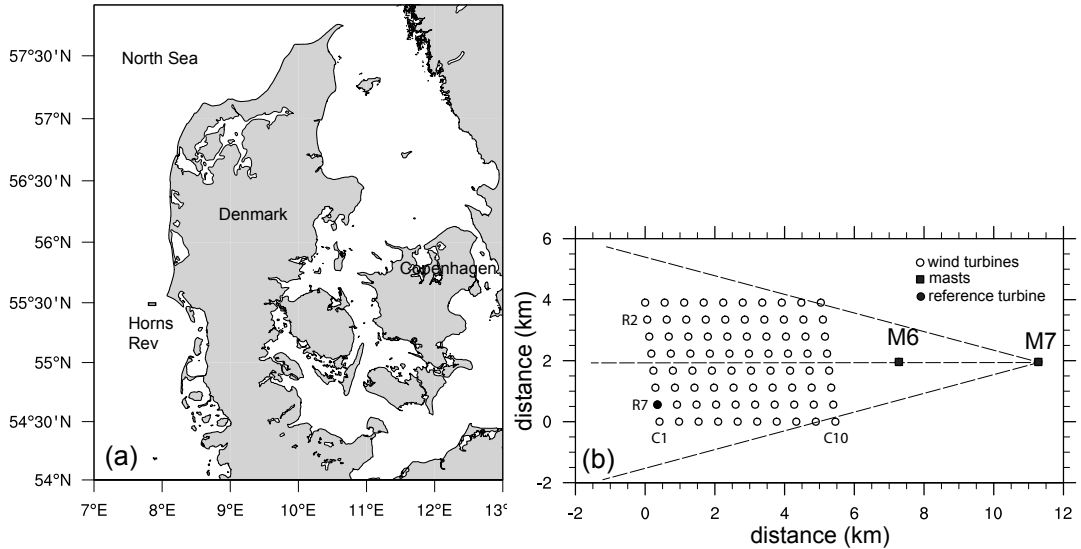
Figure 2. Location and layout of the offshore wind farm Horns Rev I including two nearby masts (M6 and M7). The centre of the wind farm and width of the sector ($\pm 15°$) used for the filtering of the measurements are indicated by the dashed lines.
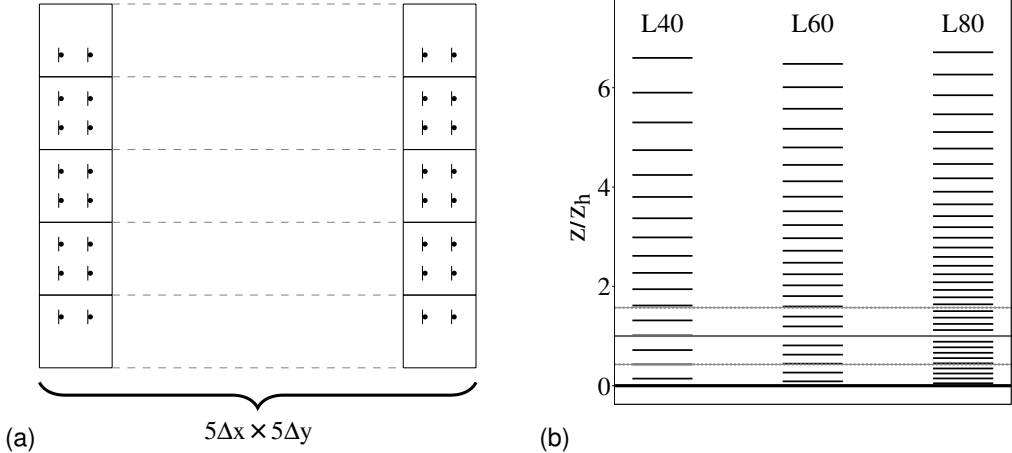
Figure 3. (a) Illustration of the model wind farm layout as applied in the mesoscale model. The squares indicate the model grid-cells and the wind turbines are marked with triangles. **(b)** Height (normalised by the turbine hub height) of the model mass-levels for the three simulations: L40, L60 and L80. The solid grey line and the dashed lines mark the hub-height and the upper and lower turbine blade tip, respectively.

37
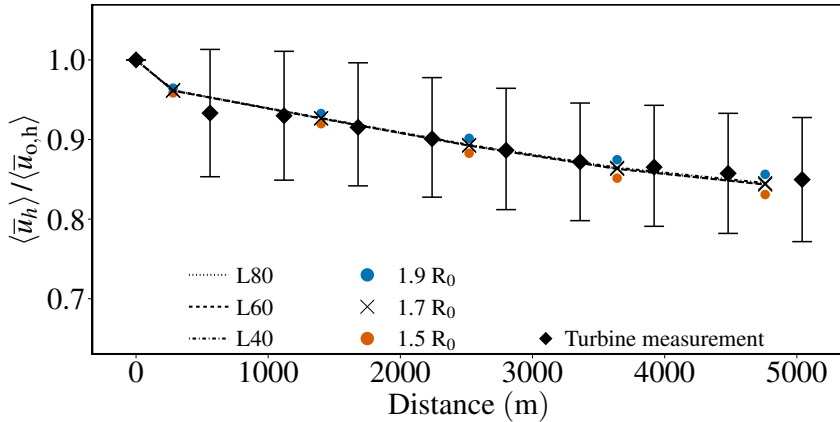
Figure 4. Measured and simulated hub-height velocity within the wind farm. The lines show the model simulated velocities averaged over wind direction with an initial length scale $\sigma_o = 1.7\, r_o$ for the 3 vertical resolutions (L40, L60, and L80). The diamonds represent the measured turbine velocity averaged over each row and the bars indicate their standard deviations. The crosses mark the velocity at the grid-cell centre. The normalised velocity for $\sigma_o = 1.5\, r_o$ and $\sigma_o = 1.9\, r_o$ is shown with red and blue dots.
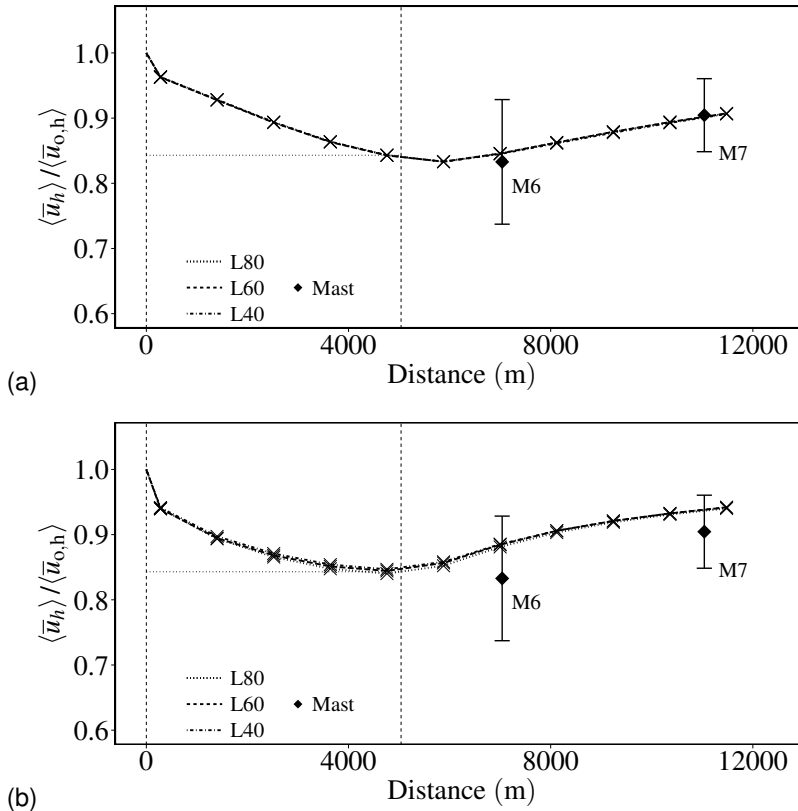
Figure 5. Hub-height velocity for the EWP **(a)** and WRF-WF **(b)** parametrisations for the L40, L60 and L80 simulations and observations as a function of distance from the western edge of the wind farm. The lines show the model simulated velocities, with the crosses showing the velocity at the grid-cell centre. The diamonds are used for the met mast measurements the bars their standard deviation. The vertical dashed lines show the wind farm extension and the horizontal dotted line the velocity with the EWP scheme at the easternmost grid-cell.
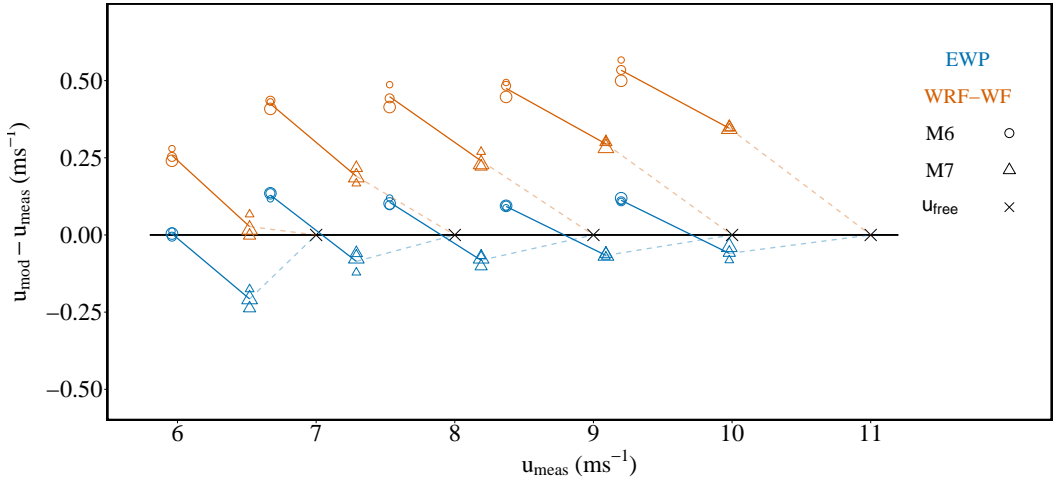
Figure 6. Modelled (u_{mod}) minus measured wind speeds (u_{meas}) at M6 (circles) and M7 (triangles) as a function of their measured wind speed, for the EWP (blue symbols) and the WRF-WF scheme (red symbols) for five wind speed bins and three vertical resolutions (symbol sizes). The coloured solid lines link the M6 and M7 values for the same wind speed bin, whereas the dashed lines the values from M7 and the free-stream velocities at the end of the wake. The crosses indicate the free-stream velocity.
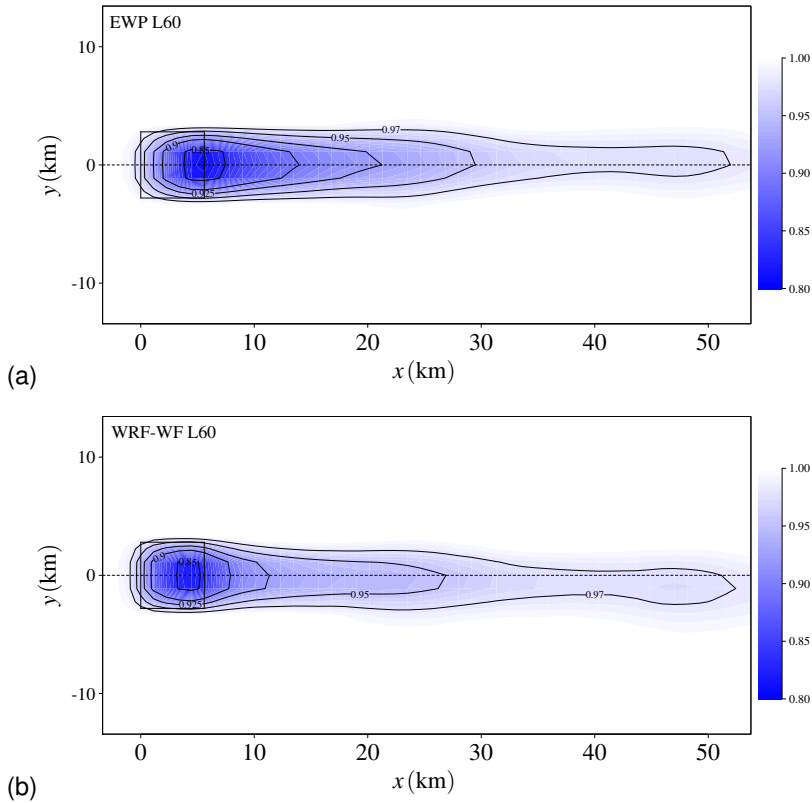
Figure 7. Horizontal view of the WRF-simulated velocity field at hub-height using the **(a)** EWP and **(b)** WRF-WF schemes. The simulations are for $10\,\mathrm{m\,s^{-1}}$ in the $270°$ wind direction and L60. The dotted line indicates the latitudinal centre and the solid rectangle the outer boundary of the wind farm.
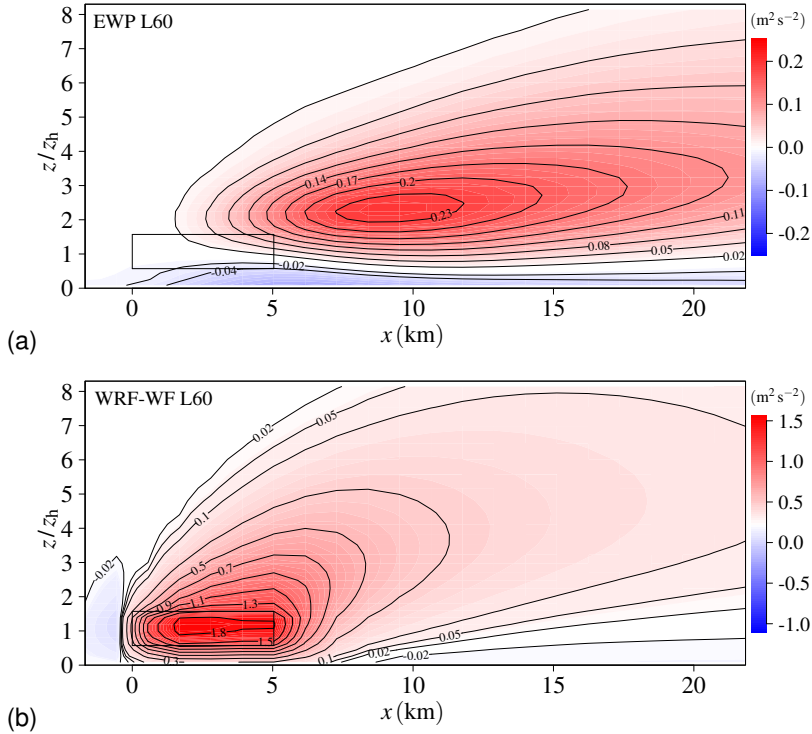
Figure 8. Vertical cross-section of the TKE difference ($\langle \overline{e}_{\text{wf}} \rangle - \langle \overline{e}_{\text{ref}} \rangle$) ($m^2\,s^{-2}$) for the simulations for $10\,m\,s^{-1}$ in the $270°$ wind direction and L60 for the **(a)** EWP and **(b)** WRF-WF scheme. The region in the model containing turbine blades is indicated by the rectangle.
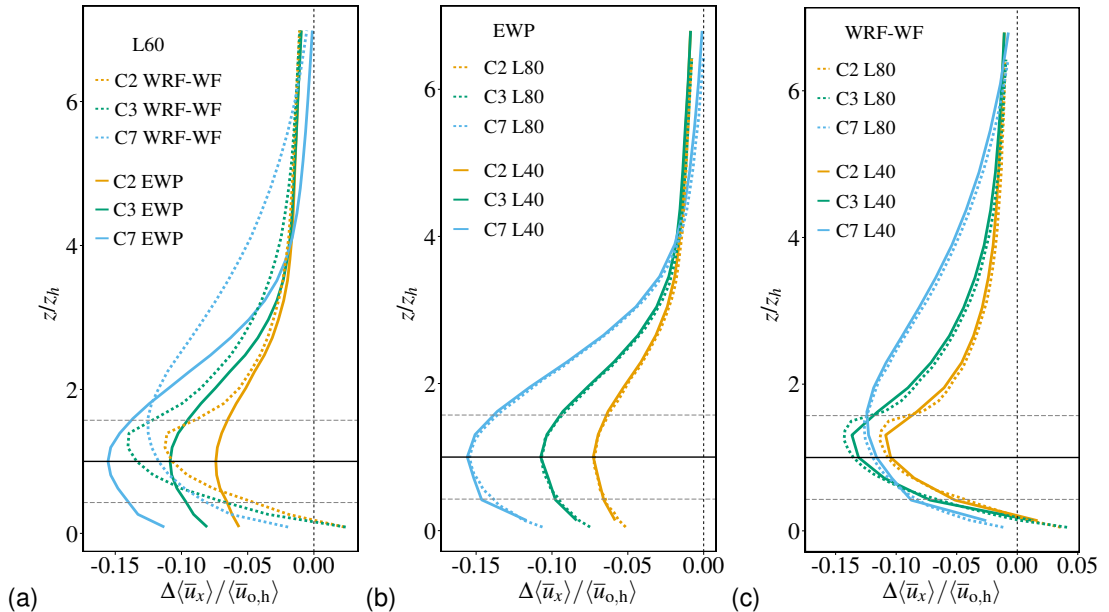
42

Figure 9. Comparison of the vertical profiles of simulated velocity deficit for the second (C2), third (C3) and seventh (C7) grid-cell containing wind turbines from the first westernmost turbine: **(a)** L60 simulations, **(b)** L40 and L80 simulation for the EWP, and **(c)** L40 and L80 simulation for the WRF-WF scheme. The turbine hub-height is indicated by the horizontal solid line and the turbine blade bottom and top by the dashed lines. The free-stream wind speed was $10\,\mathrm{m\,s^{-1}}$ in the $270°$ wind direction.
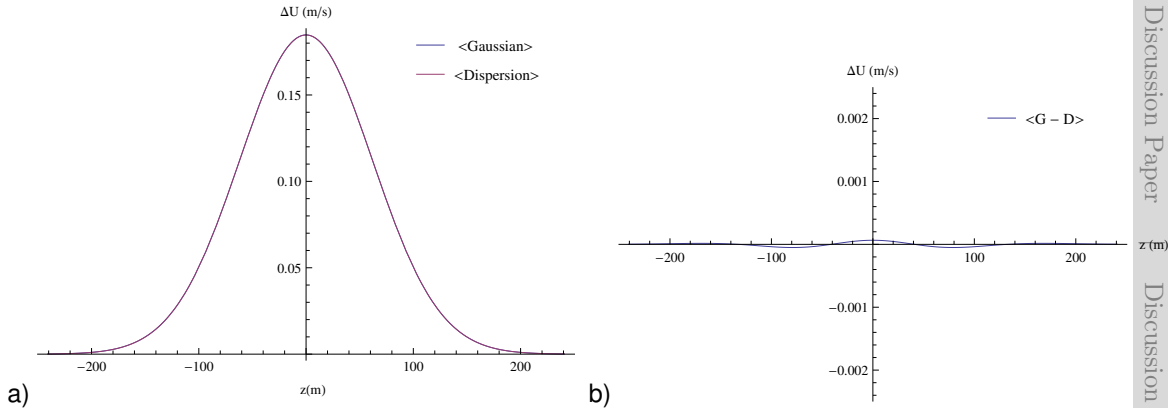
Figure 10. (a) shows a comparison between the distance average of the velocity deficit profiles (blue line) and the Gaussian profile with the average spread $\langle \sigma \rangle$ (red line). **(b)** shows the difference between the space averaged Gaussian profiles and the Gaussian profile with the average spread.